PUBLICATION V

Electromechanical interaction in eccentric-rotor cage induction machine equipped with a self-bearing force actuator

In: Journal of System Design and Dynamics 2009.
Vol. 3, No. 4, pp. 519–529.

Journal of System Design and Dynamics

Vol.3, No.4, 2009

Electromechanical Interaction in Eccentric-Rotor Cage Induction Machine Equipped with a Self-Bearing Force Actuator*

Antti LAIHO**, Kari TAMMI**, Juha ORIVUORI***, Anssi SINERVO***, Kai ZENGER*** and Antero ARKKIO***

** VTT Industrial Systems
P.O. Box 1000, FIN-02044 VTT Espoo, Finland
E-mail: antti.laiho@vtt.fi
*** Helsinki University of Technology
Faculty of Electronics, Communications and Automation, FIN-02015 TKK, Finland

Abstract

In this paper, flexural rotor vibration in a two-pole cage induction machine equipped with a built-in force actuator is examined. The built-in force actuator is based on the self-bearing machine technology in which a supplementary winding is placed in the machine for force production. The built-in force actuator enables active vibration control, but also it enables excitation of the machine for purposes of condition monitoring, for instance. A low-order parametric model is derived for the actuator-rotor system. In the model, the arbitrary eccentric rotor motion is coupled with the voltage-flux equations for the supplementary winding and eccentric rotor cage. Furthermore, based on frequency-domain system identification, a control method is examined for compensating synchronous rotor vibration. Experimental results are given for a two-pole cage induction motor. The main contribution of the article is to couple eccentric rotor motion, the built-in force actuator and the mechanical rotor model to obtain a low-order parametric model of the actuator-rotor system which can be applied to control design for rotor vibration suppression.

Key words : Rotor Vibration, Electrical Machines, Magnetic Actuator, Rotordynamics, Self-Bearing Machines, Active Control

1. Introduction

In this paper, eccentric rotor motion and flexural rotor vibration in a cage induction machine equipped with a built-in force actuator is examined. When the rotor is displaced from the stator center, the air-gap magnetic field is distorted and a net force, referred to as unbalanced magnetic pull (UMP)[(1)], is exerted on the rotor. As a result, rotordynamic characteristics of the machine change. In its extreme, the flexural rotor bending modes may couple with the electromechanical system and induce rotordynamic instability. We consider an induction machine equipped with a built-in force actuator which is based on the self-bearing machine technology[(2),(3)] in which a supplementary three-phase winding is distributed to the stator slots. When current is fed to the supplementary winding, the air-gap field is distorted and a net force is exerted on the rotor.

In this paper, a low-order parametric model is derived for the actuator-rotor system. In the model, the arbitrary eccentric rotor motion is coupled with the voltage-flux equations for the supplementary winding and eccentric rotor cage[(4)-(6)]. We present experimental results in which a test motor with extended rotor shaft is equipped with the built-in force actuator. The low-order model is identified by using vibration measurement data from the test machine. Furthermore, the built-in force actuator is applied for attenuation of flexural rotor vibration. Indeed, low-frequency vibration synchronous with the rotor rotation frequency is compensated

*Received 1 Dec., 2008 (No. 08-0838)
[DOI: 10.1299/jsdd.3.519]

by using a synchronous response control algorithm[7)–12)].

The main contribution of the paper is to couple eccentric rotor motion, the built-in force actuator and the mechanical rotor model to obtain a low-order parametric model of the system. The methodology presented provides means of model-based control design for suppression of flexural rotor vibration in electrical machines.

2. Modelling

In the following, we deduce a parametric model for a two-pole cage induction machine equipped with a supplementary four-pole winding (referred to as 'control winding') for generation of lateral force on the rotor. A single two-dimensional slice in the machine cross-section perpendicular to the rotor shaft is considered. The stator and rotor coordinate systems are depicted in Fig.1. The stator coordinate system is fixed to the stator with origin at the stator bore center. The rotor coordinate system rotates at the angular velocity of the rotor with respect to the stator coordinate system and the origins of the rotor and stator coordinate systems coincide. The rotor is rotating counter-clockwise (positive direction) with a constant angular velocity ω_m and the rotor angle $\theta_m = \theta_m(t)$, with $\dot{\theta}_m = \omega_m$, is obtained from the tachometer. Throughout the text, the quantities in stator and rotor coordinates are denoted by superscript 's' and 'r', respectively.

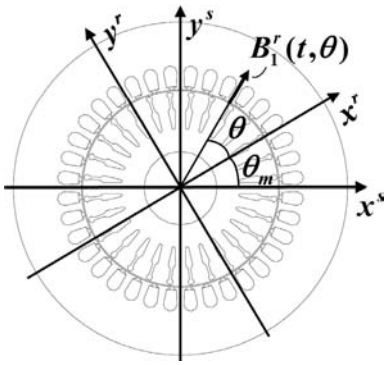

Fig. 1 Stator and rotor coordinate systems.

In this work, we use rotor coordinate system for modelling. Hence, the dominating rotordynamics related to the (synchronous) forward whirling is reduced to DC quantities. Consequently, a simplified control algorithm for vibration suppression can be used. In the following, we adopt the space-vector formalism[13)]. The space-vectors (complex-valued functions of time) are systematically denoted by underlining and equipped with a hat (^). The complex-valued variables are underlined. The space-vector of the voltage supplied to the control winding is given in the stator coordinate system by

$$\underline{\hat{u}}_c^s(t) = \frac{2}{3}\left(u_{c,a}(t) + e^{j2\pi/3}u_{c,b}(t) + e^{j4\pi/3}u_{c,c}(t)\right) \tag{1}$$

where $u_{c,a}$, $u_{c,b}$ and $u_{c,c}$ are the voltages supplied to the phases 'a', 'b' and 'c' of the control winding, respectively.

In the rotor coordinates, we have $\underline{\hat{u}}_c^r = e^{-j2\theta_m}\underline{\hat{u}}_c^s$, and by using the space-vector formalism [13)], we write the voltage-flux equations

$$\underline{\hat{u}}_c^r = R_c\underline{\tilde{i}}_c^r + \frac{\mathrm{d}\underline{\hat{\psi}}_{c,2}^r}{\mathrm{d}t} + 2j\omega_m\underline{\hat{\psi}}_{c,2}^r \tag{2}$$

$$0 = R_{r,2}\underline{\tilde{i}}_{r,2}^r + \frac{\mathrm{d}\underline{\hat{\psi}}_{r,2}^r}{\mathrm{d}t} \tag{3}$$

where R_c denotes the resistance of the control winding, $R_{r,2}$ the resistance of the rotor cage for the four-pole harmonic, $\underline{\tilde{i}}_c^r$ the current in the control winding and $\underline{\tilde{i}}_{r,2}^r$ the four-pole current

in the rotor cage. The subindex '2' refers to pole-pairs (four-pole control winding). The four-pole flux linkages of the control winding and rotor cage, $\underline{\hat{\psi}}^r_{c,2}$ and $\underline{\hat{\psi}}^r_{r,2}$ respectively, are given by

$$\underline{\hat{\psi}}^r_{c,2} = L_c \underline{\hat{i}}^r_c + M_{r,c,2} \underline{\hat{i}}^r_{r,2} + \frac{L_{c,\epsilon,2}}{2\mu_0} \underline{\hat{B}}^r_1 \underline{z}^r_r \tag{4}$$

$$\underline{\hat{\psi}}^r_{r,2} = L_{r,2} \underline{\hat{i}}^r_{r,2} + M_{r,c,2} \underline{\hat{i}}^r_c + \frac{L_{r,\epsilon,2}}{2\mu_0} \underline{\hat{B}}^r_1 \underline{z}^r_r \tag{5}$$

where L_c denotes the inductance of the control winding, $M_{r,c,2}$ the mutual inductance between the rotor cage and control winding, $L_{r,2}$ the rotor cage four-pole inductance and $\underline{z}^r_r$ the rotor center displacement measured from the stator bore center. The coordinate transformation between the rotor and stator coordinate systems (see Fig.1) is given by

$$\underline{z}^r_r = e^{-j\theta_m} \underline{z}^s_r. \tag{6}$$

Under constant-flux operational conditions, the torque-producing two-pole flux is given by

$$\underline{\hat{B}}^r_1 = \underline{B}_1 e^{j(\varphi_1 - \theta_m)} \tag{7}$$

where $\underline{B}_1$ is a complex constant and $\varphi_1 = \varphi_1(t)$ is the phase angle of the two-pole field with $\dot{\varphi}_1 = \omega_1$ in which ω_1 is the constant supply frequency of the two-pole stator winding. By using the space-vector formalism, the two-pole radial magnetic flux-density in the air-gap is given by

$$B^r_1(t,\theta) = \mathrm{Re}\left(\underline{\hat{B}}^r_1(t) e^{-j\theta}\right) \tag{8}$$

where θ is the angular coordinate along the rotor periphery (see Fig.1).

In Eqs.(4) and (5), we have used the model for eccentric rotor cage introduced by Holopainen *et al.*[4]. The model presented by Holopainen *et al.* includes the inductance $L_{r,\epsilon,2}$ induced by the eccentric rotor motion and the inductance term $L_{c,\epsilon,2}$ was here added due to the control winding.

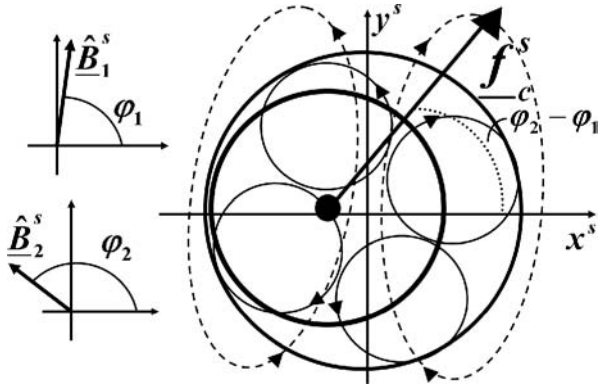

Fig. 2 Eccentric rotor motion and the force exerted on the rotor as an effect of the two-pole (dashed line) and the four-pole (solid line) fields.

The flexural net force exerted on the rotor is generated by the two-pole and four-pole fluxes in the air-gap (see Fig.2). The force exerted on the rotor is calculated from the Maxwell stress tensor[1] yielding

$$\underline{f}^r_c = \frac{\pi d_r l_r}{8\mu_0 \delta_0} |\underline{B}_1|^2 \underline{z}^r_r + \frac{\pi d_r l_r}{4\delta_0} \underline{\hat{B}}^{r*}_1 (k_{r,2} \underline{\hat{i}}^r_{r,2} + k_c \underline{\hat{i}}^r_c) \tag{9}$$

where subindex '$*$' refers to complex conjugation, d_r the rotor core diameter, l_r the rotor core axial length, $\mu_0 = 4\pi \cdot 10^{-7}$ N/A^2 permeability of vacuum, δ_0 the radial air-gap length with $k_{r,2}$ and k_c denoting the coupling factors between the currents and the generated magneto-motive forces (MMFs) of the the rotor cage and control winding, respectively. The values of the

coupling factors are related to the saturation and geometry (rotor bars, stator slots, etc.) of the rotor cage and control winding. Estimation of the system parameters is discussed later in the text.

By substituting Eq.(7) to Eq.(9), we obtain an actuator force model with periodically time-varying coefficients. However, by introducing

$$\underline{\hat{u}}^r_{c,0} = \underline{\hat{u}}^r_c e^{-j(\varphi_1-\theta_m)} \tag{10}$$

$$\underline{\hat{i}}^r_{c,0} = \underline{\hat{i}}^r_c e^{-j(\varphi_1-\theta_m)} \tag{11}$$

$$\underline{\hat{i}}^r_{r,2,0} = \underline{\hat{i}}^r_{r,2} e^{-j(\varphi_1-\theta_m)} \tag{12}$$

we obtain a linear time-invariant (LTI) model for the actuator-rotor system. We use Eq.(7) with Eqs.(10) - (12) and substitute Eqs.(4) and (5) to Eqs.(2) and (3). Furthermore, we use Eq.(7) with Eqs.(11) and (12) in Eq.(9). As a result, we obtain an electromechanical model for the actuator-rotor system as

$$\begin{aligned}\underline{\hat{u}}^r_{c,0} &= [R_c + j(\omega_1+\omega_m)L_c]\underline{\hat{i}}^r_{c,0} + j(\omega_1+\omega_m)M_{r,c,2}\underline{\hat{i}}^r_{r,2,0} + L_c\frac{\mathrm{d}\underline{\hat{i}}^r_{c,0}}{\mathrm{d}t} \\ &\quad + M_{r,c,2}\frac{\mathrm{d}\underline{\hat{i}}^r_{r,2,0}}{\mathrm{d}t} + \frac{L_{c,\epsilon,2}}{2\mu_0}\underline{B}_1[\dot{\underline{z}}^r_r + j(\omega_1+\omega_m)\underline{z}^r_r]\end{aligned} \tag{13}$$

$$\begin{aligned}0 &= [R_{r,2} + j(\omega_1-\omega_m)L_{r,2}]\underline{\hat{i}}^r_{r,2,0} + j(\omega_1-\omega_m)M_{r,c,2}\underline{\hat{i}}^r_{c,0} + L_{r,2}\frac{\mathrm{d}\underline{\hat{i}}^r_{r,2,0}}{\mathrm{d}t} \\ &\quad + M_{r,c,2}\frac{\mathrm{d}\underline{\hat{i}}^r_{c,0}}{\mathrm{d}t} + \frac{L_{r,\epsilon,2}}{2\mu_0}\underline{B}_1[\dot{\underline{z}}^r_r + j(\omega_1-\omega_m)\underline{z}^r_r]\end{aligned} \tag{14}$$

$$\underline{f}^r_c = \frac{\pi d_r l_r}{8\mu_0\delta_0}|\underline{B}_1|^2\underline{z}^r_r + \frac{\pi d_r l_r}{4\delta_0}\underline{B}^*_1(k_{r,2}\underline{\hat{i}}^r_{r,2,0} + k_c\underline{\hat{i}}^r_{c,0}) \tag{15}$$

$$m\ddot{\underline{z}}^r_r + (c + 2jm\omega_m)\dot{\underline{z}}^r_r + (k - m\omega_m^2 + jc\omega_m)\underline{z}^r_r = \underline{f}^r_c + \underline{f}^r_{ex}. \tag{16}$$

The input of the system is the voltage $\underline{\hat{u}}^r_{c,0}$ supplied to the control winding with the disturbance force $\underline{f}^r_{ex}$. The states of the system are the currents in the control winding $\underline{\hat{i}}^r_{c,0}$ and the rotor cage $\underline{\hat{i}}^r_{r,2,0}$ with rotor radial position $\underline{z}^r_r$ being the measurable output. For a given voltage demand $\underline{\hat{u}}^r_{c,0}$, the actual 3-phase voltage supply $\underline{\hat{u}}^s_c$ to the control winding given by Eq.(1) is realized in the stator coordinate system as

$$\underline{\hat{u}}^s_c = e^{j2\theta_m}\underline{\hat{u}}^r_c = e^{j(\varphi_1+\theta_m)}\underline{\hat{u}}^r_{c,0}. \tag{17}$$

In Eq.(16), the Jeffcott rotor model is written in the rotor coordinate system[14]. In the rotor model, m is the (modal) mass of the rotor, c the damping coefficient and k the stiffness coefficient of the rotor. Furthermore, the external excitation force $\underline{f}^r_{ex}$ is typically dominated by the rotor rotation harmonics.

The actuator-rotor system given by Eqs.(13) - (16) can be formulated as a standard LTI system in the complex form as

$$\dot{\underline{q}}^r = \underline{A}\,\underline{q}^r + \underline{B}\,\underline{\hat{u}}^r_{c,0} \tag{18}$$

$$\underline{z}^r_r = \underline{C}\,\underline{q}^r \tag{19}$$

where the complex state vector is given by

$$\underline{q}^r = \begin{pmatrix} \dot{\underline{z}}^r_r \\ \underline{z}^r_r \\ \underline{\hat{i}}^r_{c,0} \\ \underline{\hat{i}}^r_{r,2,0} \end{pmatrix}.$$

3. Rotor Vibration Control

For the actuator-rotor system, the convergent control (CC) algorithm[15] is here applied for attenuation of vibration originated from periodic excitations. For the mass unbalance

compensation of the first rotation speed harmonic, the CC algorithm simplifies in the rotor coordinate system to

$$\hat{\underline{u}}^r_{c,0}(n) = \gamma_0 \hat{\underline{u}}^r_{c,0}(n-1) - \alpha_0 h_{\mathbb{C}}^{-1} \underline{z}^r_r(n). \tag{20}$$

In Eq.(20), n refers to the time instant $t_n = nT_s$ with T_s denoting the sample time. Furthermore, the complex number $h_{\mathbb{C}}$ given by

$$h_{\mathbb{C}} = -\underline{C}\,\underline{A}^{-1}\,\underline{B} \tag{21}$$

is the DC frequency-response of the actuator-rotor system in Eqs.(18) and (19). Furthermore, $0 < \gamma_0 \leq 1$ and $\alpha_0 > 0$ are parameters related to the convergence of the algorithm.

In the case of a negligible slip ($\omega_1 = \omega_m$), as can be seen from Eq.(14), the rotor cage currents disappear from the DC frequency-response. In this case, the DC frequency-response obtained from Eqs.(13) - (16) is given by

$$h_{\mathbb{C}} = \frac{\pi d_r l_r}{4\delta_0} \frac{k_c \underline{B}_1^*}{(R_c + j2\omega_1 L_c)(k - m\omega_1^2 + jc\omega_1 - k_0) + 2jk_0 k_c \omega_1 L_{c,\epsilon,2}} \tag{22}$$

where

$$k_0 = \frac{\pi d_r l_r}{8\mu_0 \delta_0} |\underline{B}_1|^2$$

denotes the (negative) spring constant related to the radial UMP.

4. Experimental Set-Up

A two-pole 30 kW cage induction motor (see Fig.3) was used in experiments. The motor was equipped with an extended rotor shaft (length 1560 mm, total weight with rotor stack 55.8 kg) with the first rotor bending mode being at 36.9 Hz (damping ratio 0.76%). The modal data was obtained from the experimental modal testing[16] which was carried out for the rotor. The control winding for force production was a four-pole three-phase winding with 40 turns in each phase. Eddy-current displacement transducers were attached at the driving end of the machine close to the end-shield. In addition, two coils were installed in the stator slots in order to measure the two-pole flux.

During the experiments, the machine was run without load at 30.0 Hz (rated 50 Hz) and 74.4 V / 6.0 A (rated 400 V / 50 A) supply in the torque-producing two-pole winding. This gave a two-pole magnetic flux density of 0.37 T (measured with two-pole flux measurement windings). Even though the machine was run without load, a small slip of $2.47 \cdot 10^{-2}$ rad/s ($s = (\omega_1 - \omega_m)/\omega_1 = 0.013\%$) due to the cooling fan and friction was recorded. Due to the slip, the rotor displacement fluctuated. In the identification, the effect of the control $\hat{\underline{u}}^r_{c,0}$ on the rotor displacement was calculated by subtracting the uncontrolled displacement from the controlled displacement[17].

The online signal processing was performed by using dSpace system operating in SIMULINK environment by using MATLAB Real Time Workshop. The sampling frequency was

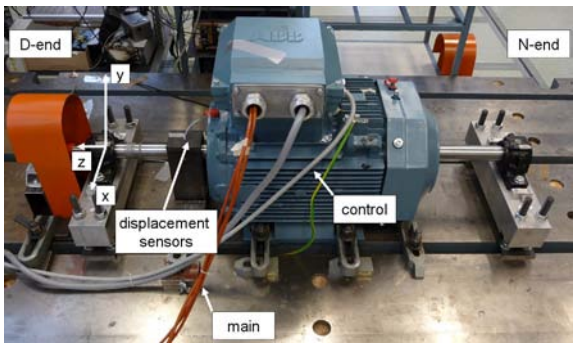

Fig. 3 The test machine used in experiments.

set to 5 kHz. The displacement measurements $\underline{z}_r^s$ were supplied to dSpace system. The control signal $\underline{\hat{u}}_{c,0}^r$ was obtained from CC algorithm by using the coordinate transformation given by Eq.(6) and the adaptation given by Eq.(20). The signal was amplified and supplied to the control winding.

Table 1 Parameters related to the DC frequency-response given by Eq.(22).

parameter	description	value	unit
d_r	diameter of rotor core	190.0	mm
l_r	length of rotor core	180.0	mm
N_c	number of turns per phase in control winding	40	1
p_c	number of pole pairs in control winding	2	1
δ_0	radial air-gap length	1.0	mm
$\arg(\underline{B}_1)$	initial phase angle of two-pole flux	120	deg
$\lvert\underline{B}_1\rvert$	peak value of two-pole flux	0.37	T
ω_1	supply frequency of main winding	$2\pi \cdot 30.0$	rad/s
k_c	coupling factor of control winding	15.0	1
R_c	resistance of control winding	14.8	Ω
L_c	inductance of control winding	27.0	mH
$L_{c,\epsilon,2}$	eccentricity-inductance of control winding	$1.27 - 7.35j$	mH
ω_0	natural frequency of rotor	$2\pi \cdot 36.9$	rad/s
ξ	damping ratio of rotor	0.76	%
m	modal mass of rotor	147.0	kg
k	modal stiffness of rotor	7.9	MN/m
c	modal damping of rotor	517.9	Ns/m

5. Results

In order to validate the modelling, the frequency response of the actuator-rotor system was determined from the analytical expression given by Eq.(22). The parameters in Eq.(22) are listed in Table 1. The mechanical parameters ω_0, ξ and m were obtained directly from the modal testing carried out for the rotor. Hence, k and c were given by $k = m\omega_0^2$ and $c = 2\xi\omega_0 m$. The phase angle of the fundamental two-pole field, $\arg(\underline{B}_1)$, was fixed by the difference between the trigger point of the tacho ($\theta_m = 0$ in Fig.1) and the main axis of the two-pole flux measurement winding. The parameters k_c and L_c were obtained from the machine geometry by $k_c = 3N_c/(4p_c)$ and $L_c = \mu_0 \pi d_r l_r N_c^2/(8\delta_0)$, respectively[18]. In order to obtain the parameters, sinusoidal distribution of the control winding MMF was assumed. In addition, the effect of stator slotting and saturation of magnetic materials was neglected. A measured value was used for the control winding resistance R_c. As well, based on Eqs.(13) and (14) with $\omega_1 = \omega_m$, the inductance $L_{c,\epsilon,2}$ was obtained from measurements by supplying DC voltage in rotor coordinates to the control winding and measuring the DC responses for the rotor displacement and currents in the control winding. By substituting the parameters listed in Table 1 to Eq.(22), the DC frequency response is obtained as

$$h_{\mathbb{C}} = \underline{z}_r^r / \underline{\hat{u}}_{c,0}^r = 1.8 \cdot e^{-j\pi \cdot 137.1/180} \ (\mu\text{m/V}). \tag{23}$$

In the experimental system identification, DC voltage supply $\underline{\hat{u}}_{c,0}^r = 16.0 \cdot e^{-j\pi \cdot 30/180}$ (V) to the control winding was used. The DC displacement $\underline{z}_r^r = 110.0 \cdot e^{-j\pi \cdot 161.8/180}$ (μm) was measured from which the FRF

$$h_{\mathbb{C}} = \underline{z}_r^r / \underline{\hat{u}}_{c,0}^r = 6.9 \cdot e^{-j\pi \cdot 131.8/180} \ (\mu\text{m/V}) \tag{24}$$

was obtained. The absolute value of the measured FRF in Eq.(24) is almost four times higher than the one given by Eq.(23). The phase error between the calculated and measured FRFs is 5.3 deg.

The CC algorithm given by Eq.(20) was applied with parameters $\gamma_0 = 1.0$ and $\alpha_0 = 2.0 \cdot 10^{-4}$. The DC response $h_{\mathbb{C}}$ from Eq.(24) was used in the adaptation loop. In Fig.4 the rotor orbit is shown when the control was switched on at $t = 0.7$ s. The vibration amplitudes (rms) reduced from 176.0 μm to 18.0 μm (x -direction) and from 146.0 μm to 17.0 μm (y -direction). The steady-state rotor orbits with control off and control on are shown in Fig.5.

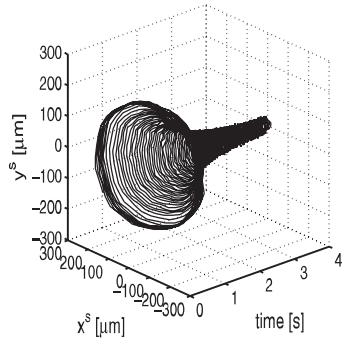

Fig. 4 Rotor orbit when the control was switched on.

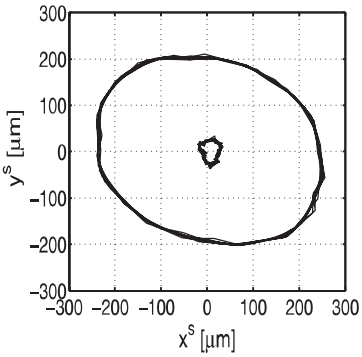

Fig. 5 Rotor orbit at the steady-state conditions with control off (outer orbit) and control on (inner orbit).

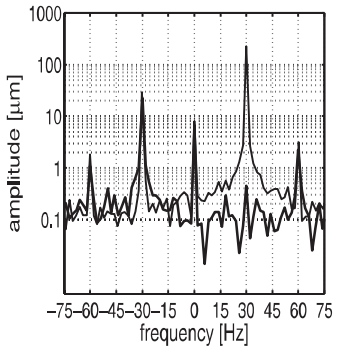

Fig. 6 Spectrum of the steady-state rotor displacement $\underline{z}_r^s$ with control off (thin line) and control on (thick line).

Table 2 Dominating spectral components of the rotor displacement $\underline{z}_r^s$.

frequency [Hz]		control off [μm]	control on [μm]
-30	(backward whirling)	30.0	23.0
0	(DC)	8.0	7.0
30	(forward whirling)	226.0	0.5

The spectrum of the rotor displacement in the stator coordinate system is shown in Fig.6. The data of the dominating peaks at −30 Hz, 0 Hz and 30 Hz is listed in Table 2. The results show that the forward whirling component is suppressed effectively. Consequently, the rotor changes from forward whirling to backward whirling.

In Fig.7, with control on, the steady-state voltage supply $\underline{\hat{u}}_{c,0}^r$ to the control winding is shown. Real and imaginary parts of the control were 24.36 V and -12.44 V, respectively. As can be seen from the longer time history in Fig.8, the supply voltage fluctuates due to the slip. The measured current in the control winding phase 'a' is shown in Fig.9. The rms values for the current is 0.32 A (control off) and 0.13 A (control on).

In Fig.10, spectrum of the steady-state control winding current $\underline{\hat{i}}_c^s$ is shown for the un-

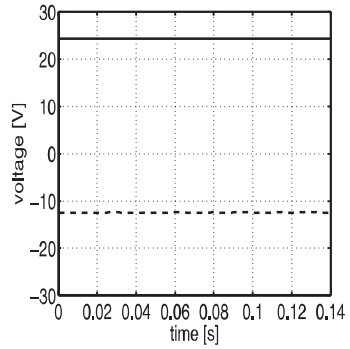

Fig. 7 Control winding supply $\underline{\hat{u}}^r_{c,0}$; real part (solid line) and imaginary part (dashed line).

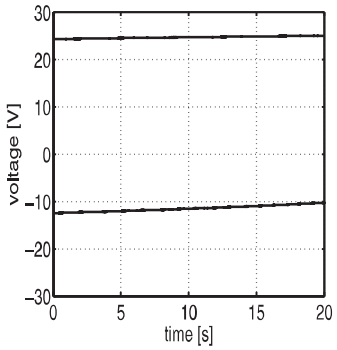

Fig. 8 Fluctuation of the control winding supply $\underline{\hat{u}}^r_{c,0}$ due to the slip; real part (above) and imaginary part (below).

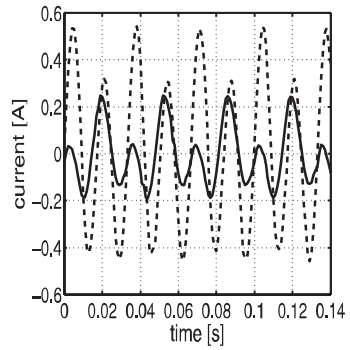

Fig. 9 Current in the control winding phase 'a' with control off (dashed line) and control on (solid line).

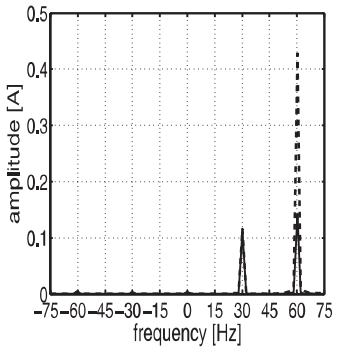

Fig. 10 Spectrum of the steady-state control winding current $\underline{\hat{i}}^s_c$ with control off (dashed line) and control on (solid line).

controlled and controlled system. Data of the dominating peaks is listed in Table 3. In the uncontrolled case, the major two peaks at 30 Hz and 60 Hz are induced by DC and forward

Table 3 Dominating spectral components of the control winding current $\hat{\underline{i}}_c^s$.

frequency [Hz]	control off [A]	control on [A]
30	0.12	0.11
60	0.43	0.14

whirling components of $\underline{z}_r^s$, respectively (see Table 2). Indeed, from Eq.(13) we see that $\underline{z}_r^r$ component rotating with angular frequency $\omega - \omega_m$ ($\underline{z}_r^s$ rotating with ω) induces $\hat{\underline{i}}_{c,0}^r$ rotating with the same frequency. By using Eq.(11), we obtain

$$\hat{\underline{i}}_c^s = e^{j2\theta_m}\hat{\underline{i}}_c^r = e^{j(\theta_m+\varphi_1)}\hat{\underline{i}}_{c,0}^r.$$

Consequently, $\underline{z}_r^s$ rotating with ω induces $\hat{\underline{i}}_c^s$ rotating with $\omega + \omega_1 \approx \omega + \omega_m$ when slip is negligible. Furthermore, from Eq.(13), we see that $\underline{z}_r^r$ component rotating with angular frequency $-(\omega_1 + \omega_m) \approx -2\omega_m$ does not induce current in the control winding. By using Eq.(6) we see that, with a negligible slip, the component is the backward whirling component in the stator coordinate system. Current is not induced in the control winding due to the fact that the four-pole flux induced by the backward whirling is static with respect to the control winding.

From Fig.6 and Table 2, we see that the forward whirling component was reduced effectively when the control was switched on. Hence, as can be seen from Fig.10 and Table 3, the 60 Hz current component was reduced.

6. Discussion and Conclusions

In this paper, flexural rotor vibration in a two-pole cage induction machine equipped with a supplementary winding based on self-bearing technology was considered. A low-order parametric model was deduced for the actuator-rotor system under eccentric rotor motion. The model was used to estimate the system frequency response. On the other hand, the actuator-rotor system was identified in the frequency domain by using measurement data of a two-pole 30 kW cage induction motor. The measured and calculated FRFs agree in terms of the phase angle (difference 5.3 deg) which is important for the stability of the controlled system. On the other hand, the amplitude of the measured and calculated FRFs differ considerably (almost by factor 4). This is most probably due to the non-isotropic bearings, saturation of magnetic materials and stator and rotor slotting which were not included in the model. However, in terms of the used convergent control algorithm, the stability of the controlled system is determined by the phase error[19), (20)].

Based on the identification, a control algorithm was used for attenuation of (synchronous) forward whirling of the rotor. The results show that a considerable level of flexural rotor vibration suppression (89.4% reduction in amplitude) can be achieved by compensating the dominant vibration component. The rotor coordinate formalism applied in this work provides a straightforward identification and control of the rotor forward whirling. However, for controlling the backward rotor whirling and other harmonics, a more comprehensive synchronous response control has to be considered.

The built-in force actuator provides means of producing a controlled force on the rotor. In this paper, the force actuator was applied for vibration attenuation and its efficiency was shown. The built-in force actuator may also be used for condition monitoring or fault diagnostics: i) the machine can be excited with the actuator and the responses monitored, ii) the currents induced in the control winding can be used as signatures of possible faults, iii) control commands may be monitored as indicators of changes in machine state, analogically to the methodology used in active magnetic bearings.

Acknowledgements

The authors gratefully acknowledge financial support from the Academy of Finland and VTT Technical Research Centre of Finland. Special thanks are devoted to Prof. Marko Hinkkanen, Helsinki University of Technology, Power Electronics Laboratory, for guidance

with the dSpace system. The authors are grateful to Mr. Ari Haavisto, Helsinki University of Technology, Faculty of Electronics, Communications and Automation, for assistance in experiments and building up the experimental set-up.

References

(1) A. Smith, D. Dorrell, Calculation and measurement of unbalanced magnetic pull in cage induction motors with eccentric rotors. part i: Analytical model, IEE Proceedings – Electric Power Applications 143(3) (1996) 193–201.

(2) A. Chiba, D. T. Power, M. A. Rahman, Characteristics of a bearingless induction motor, IEEE Transactions on Magnetics 27(6) (1991) 5199–5201.

(3) A. Chiba, T. Fukao, M. Rahman, Vibration suppression of a flexible shaft with a simplified bearingless induction motor drive, Conference Record of the 2006 IEEE Industry Applications Conference 2006. 41st IAS Annual Meeting. 2 (2006) 836–842.

(4) T. P. Holopainen, A. Tenhunen, E. Lantto, A. Arkkio, Unbalanced magnetic pull induced by arbitrary eccentric motion of cage rotor in transient operation, part 1: Analytical model, Electrical Engineering (Archiv für Electrotechnik) 88(1) (2005) 13–24.

(5) A. Laiho, K. Tammi, K. Zenger, A. Arkkio, A model-based flexural rotor vibration control in cage induction electrical machines by a built-in force actuator, Electrical Engineering (Archiv für Electrotechnik) 90(6) (2008) 407–421.

(6) A. Laiho, K. Tammi, J. Orivuori, A. Sinervo, K. Zenger, A. Arkkio, Electromechanical interaction in eccentric-rotor cage induction machine equipped with a self-bearing force actuator, Proceedings of the Eleventh International Symposium on Magnetic Bearings (ISMB11), Nara, Japan, August 26-29, 2008.

(7) C. R. Burrows, M. N. Sahinkaya, Vibration control of multi-mode rotor-bearing systems, Proceedings of the Royal Society of London, Series A, Mathematical and Physical Sciences 386(1790) (1983) 77–94.

(8) L. Sievers, A. von Flotow, Linear control design for active vibration isolation of narrow band disturbances, Proceedings of the 27th IEEE Conference on Decision and Control 2 (1988) 1032–1037.

(9) S. Hall, N. Wereley, Linear control issues in the higher harmonic control of helicopter vibrations, Proceedings of 45th Annuual Forum of the American Helicopter Society, Boston, USA (1989) 955–971.

(10) C. Knospe, R. Hope, S. Fedigan, R. Williams, New results in the control of rotor synchronous vibration, Proceedings of the Fourth International Symposium on Magnetic Bearings (ISMB4), vdf Hochschulverlag AG, Zurich, Switzerland, August 23-26, 1994.

(11) P. S. Keogh, C. R. Burrows, T. Berry, On-Line Controller Implementation for Attenuation of Synchronous and Transient Rotor Vibration, Journal of Dynamic Systems, Measurement, and Control 118 (1996) 315–321.

(12) E. Lantto, Robust control of magnetic bearings in subcritical machines, Doctoral dissertation. Acta Polytechnica Scandinavica, The Finnish academy of technology (http://lib.tkk.fi/Diss/199X/isbn9512255758/) 1–143, 1999.

(13) P. K. Kovács, Transient phenomena in electrical machines, Elsevier Science Publishers, Amsterdam, 1984.

(14) G. Genta, Dynamics of rotating systems, Springer-Verlag New York, Inc., 2005.

(15) C. Knospe, S. Fedigan, R. W. Hope, R. Williams, A multitasking dsp implementation of adaptive magnetic bearing control, IEEE Transactions on Control Systems Technology 5(2) (1997) 230–238.

(16) D. Ewins, Modal Testing: Theory and Practise, Advanced Studies Press, London, 2000.

(17) A. Sinervo, Modeling and control of flexural rotor vibration of a two-pole cage induction motor, Master's thesis, Helsinki University of Technology, Faculty of electronics, Communications and Automation, Department of electrical Engineering, Espoo, Finland (2008).

(18) J. Chiasson, Modeling and high-performance control of electric machines, John Wiley & Sons, Inc., 2005.
(19) C. Knospe, R. Hope, S. Tamer, S. Fedigan, Robustness of adaptive unbalance control of rotors with magnetic bearings, Journal of Vibration and Control 2 (1996) 33–52.
(20) K. Tammi, Active control of radial rotor vibrations: Identification, feedback, feedforward, and repetitive control methods, Doctoral dissertation, Helsinki University of Technology, Department of Automation and Systems Technology (http://lib.tkk.fi/Diss/2007/isbn9789513870089/) 1–165, 2007.